

# Measurement of the stray field emanating from magnetic force microscope tips by Hall effect microsensors

A. Thiaville<sup>a)</sup> and L. Belliard

Laboratoire de Physique des Solides, Centre National de la Recherche Scientifique,  
Université Paris-Sud, 91405 Orsay, France

D. Majer and E. Zeldov

Department of Condensed Matter Physics, Weizmann Institute of Science, 76100 Rehovot, Israel

J. Miltat

Laboratoire de Physique des Solides, Centre National de la Recherche Scientifique,  
Université Paris-Sud, 91405 Orsay, France

(Received 8 January 1997; accepted for publication 25 June 1997)

We describe the use of micronic Hall sensors as magnetic-field profilometers with submicron resolution. The procedure involves the deconvolution of Hall voltage maps produced by scanning the field source over the sensor, with a scanning probe microscope. The response function of an infinite Hall cross is calculated analytically in the two-dimensional case, using conformal mapping techniques. Various methods of deconvolution of the Hall voltage maps are presented and compared. The calculated response function is used for the deconvolutions, and different effective sensor sizes are tried. It is shown that the remaining main uncertainties come from the ignorance of the true response function of the sensor, ascribed to the charge depletion phenomenon that is known to occur at the sensor edges. The method is applied to thin-film magnetic force microscope tips for which a precise knowledge of the tips field at sample location proves crucial to image interpretation. Maximum fields in the range 10–100 Oe are found at a distance known to be about 100 nm from the tip contact surface, depending on the tip coating thickness and magnetization direction.  
© 1997 American Institute of Physics. [S0021-8979(97)03919-4]

## I. INTRODUCTION

Magnetic force microscopy (MFM) is being increasingly used as a high-resolution magnetic microscope.<sup>1</sup> Compared to the Kerr effect or Faraday effect magneto-optical microscopy, its main advantage is increased resolution: resolution better than 0.1  $\mu\text{m}$  is routinely achieved. Compared to electron-based imaging techniques, MFM requires virtually no sample preparation. The price to be paid, however, is, besides the cost of the microscope itself, the difficulty of interpreting the images. Whereas in Kerr microscopy, the polar, longitudinal, and transverse geometries allow a direct estimation of the magnetization vector orientation,<sup>2</sup> the contrast formation mechanism in MFM is more complex, so that no immediate translation of the MFM picture in terms of a magnetization vector distribution can be performed.

In a first approximation, nevertheless, wherein the magnetic states of the sample and tip are assumed not to be perturbed, the MFM contrast stems from the first (static mode) or second (vibrating tip mode) derivative, with respect to the distance to the sample, of the sample tip stray field times the tip magnetization.<sup>1</sup> Equivalently,<sup>3</sup> the contrast arises from the dot product of the tip stray field with the sample magnetization.

A frequent procedure consists in preparing tips covered with a hard magnetic material, thus, minimizing the risk of a modification of the magnetic structure of the tip. These hard tips may also be magnetized in different directions, allowing the various components of the sample stray field to be

measured.<sup>4</sup> If one then uses the second formulation of the interaction it becomes clear that for the contrast to be high, the tip stray field has to be large, but then the sample may be too much disturbed. The tip stray field here, becomes a key parameter in the trade off between sensitivity and sample disturbance. Its lateral extension influences the resolution of the microscope (at a given flying height), its value determines the contrast and the “aggressivity” of the microscope. It ought also to be noted that one of the promising approaches to MFM simulation is to calculate how the sample responds to the tip field while scanning the tip.<sup>5</sup> Therefore, tip characterization is essential, be it as a tool for development of better tips, or as an input to simulation.

A number of techniques have already been employed for this purpose. The stray field around the tip has been imaged by Lorentz microscopy in a (scanning) transmission electron microscope, in the Foucault,<sup>6</sup> differential phase contrast,<sup>7</sup> and electron holography<sup>8,9</sup> modes. The last two methods are quantitative, but give only access to integrals along the beam direction of one or two transverse field components. As discussed in Ref. 8, obtaining by the last technique a field map in the sample plane is still not easy. Tip field measurements by magnetoresistive heads<sup>10</sup> have also been performed, but have not been quantified and were, moreover, unidimensional due to the large track width.

In this paper, we propose another measurement technique, which employs a Hall effect sensor patterned by microlithography to a micron-size cross. Such small Hall sensors were first used by Chang *et al.* as local field sensors in their scanning Hall probe microscope.<sup>11</sup> Here, we invert the

<sup>a)</sup>Electronic mail: thiav@lps.u-psud.fr

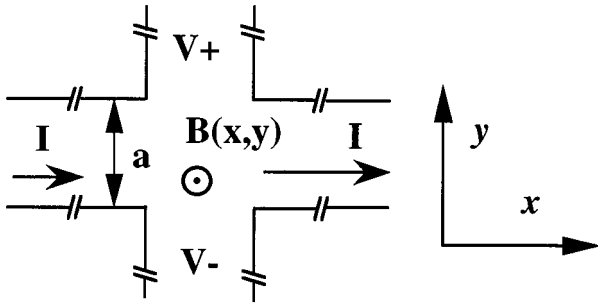


FIG. 1. Schematic and definitions for a Hall sensor shaped as an infinite arms cross.

geometry, put the Hall sensor as the MFM sample, and scan the MFM tip over it while recording the Hall voltage, thus, creating a Hall voltage map. We shall present experimental results first, then develop a calculation of the response of the Hall sensor to a nonuniform magnetic field. The following section will be devoted to the deconvolution procedure essential to the conversion of the Hall voltage map into a tip field map. Finally, some practical applications of the methods developed are presented and discussed.

## II. EXPERIMENTAL METHOD AND RESULTS

The Hall sensors were fabricated by lithography on GaAs/AlGaAs heterostructures. These are grown by molecular beam epitaxy in a Riber model 32 system under conventional growth conditions. A  $1\ \mu\text{m}$  thick buffer layer is first grown on the (001) oriented, semi-insulating GaAs substrate beginning with a short superlattice followed by undoped GaAs. A 10 nm thick AlGaAs spacer isolates between the two-dimensional electron gas and the ionized impurities. A delta doped region of density  $10^{12}\ \text{cm}^{-2}$  is used to supply the carriers to the two-dimensional (2D) electron gas, which further extends into a 25 nm AlGaAs layer, uniformly doped to  $10^{18}\ \text{cm}^{-3}$ . Nominally, 35% Al is used in these AlGaAs layers and a relatively low Si concentration, in order to ensure a complete freeze-out of the excess carriers when the sensors are used at low temperatures (the freeze-out occurs below about 100 K). The Al concentration is then ramped down towards the surface to 25% over 25 nm also doped to  $10^{18}\ \text{cm}^{-3}$ . A 25 nm GaAs cap layer doped to  $5 \times 10^{17}\ \text{cm}^{-3}$  protects the surface. This structure was chosen in order to facilitate the formation of low-resistivity Ohmic contacts and to avoid creeping and deterioration due to surface oxidation. The etch depth in the lithographic process is 100 nm. The structure of the sensors consists of ten Hall crosses (Fig. 1), with a width of about  $2.2\ \mu\text{m}$  [atomic force microscopy (AFM) data], and a device resistance in the  $20\ \text{k}\Omega$  range at room temperature. In these nonmagnetic sensors, only the normal Hall effect exists: the sensor responds to the field perpendicular to its plane. The sensor sensitivity, at room temperature, was about  $70\ \text{m}\Omega/\text{G}$  in a uniform field. As the sheet resistance of the sensors is  $1\ \text{k}\Omega/\text{square}$ , the Hall mobility at room temperature amounts to  $7000\ \text{cm}^2\ \text{V}^{-1}\ \text{s}^{-1}$ . A dc current source applies a  $100\ \mu\text{A}$  current, resulting in a  $7\ \mu\text{V}$  Hall voltage for a 1 Oe spatially uniform perpendicular

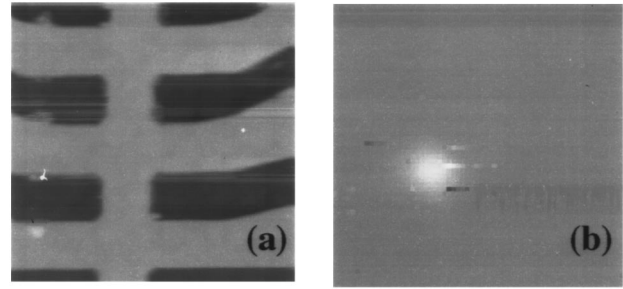


FIG. 2. Time sequence of (a) an AFM scan ( $13.3\ \mu\text{m}$  size) over the sensors; (b) a Hall voltage map ( $13.6\ \mu\text{m}$  size,  $64 \times 64$  points) from roughly the same place. Axial tip magnetization, feed current 0.1 mA, and maximum signal 0.2 mV.

field. The effective sensor width, across which the current flows, is not so easy to determine. It is known that the surface states created during the patterning process on the edges of the sensor cause some charge depletion near the borders, reducing the sensor effective width. A frequent estimate<sup>12</sup> for the depleted width is  $0.1\ \mu\text{m}$ , resulting in a sensor width estimation of about  $2\ \mu\text{m}$ .

We used in the present experiments a Nanoscope III microscope from Digital Instruments. Tips are commercially available (NanoProbe<sup>TM</sup>) pyramids etched in Si cantilevers. They were sputter covered by a thin layer of a  $\text{Co}_{80}\text{-Cr}_{20}$  alloy (dc sputtering, Ar pressure  $\approx 0.1$  mbar, sputtering power  $3\ \text{W}/\text{cm}^2$ , at room temperature), of varying thickness (between 30 and 170 nm). Glass coupons sputtered together with the tip showed that the sample plane was magnetically easier, with a coercive field about 500 Oe. The images were taken in the AFM contact mode, with no tip vibration.

Let us first demonstrate how the measurement technique may be implemented by showing some typical results. Figure 2(a) displays a topographic AFM scan over the sensor, and Fig. 2(b) is a Hall voltage map acquired just after, at low resolution with a mesh size of  $0.21\ \mu\text{m}$  with the same tip, magnetized along the pyramid axis, while scanning roughly the same region. Due to synchronization problems, it was impossible to acquire the Hall voltage simultaneously with the AFM topographic scan. But, clearly, a signal appears only when the tip is positioned over the sensor.

Figure 3 shows four Hall maps, at high resolution with a mesh size of  $0.1\ \mu\text{m}$ , acquired with the same tip, as it was magnetized axially in the two senses, and in the two transverse directions. The Hall maps are fully consistent with what can be expected from a dipolar tip, with the dipole oriented along the magnetizing field. This shows directly that a ‘‘hard’’ tip can, indeed, be fabricated. One notices also that the Hall voltages are weaker for the transversely magnetized tips, a feature which can be understood from the tip pyramidal geometry. Consider, indeed, the extreme case of a tip shaped as a blade, for which the magnetization in each of the two facets lies along the projection of the magnetizing field onto the facet plane. An axial field will create a tip magnetic configuration with poles at the blade edge and opposite poles on the backside of the blade, which are far from a sample, producing, consequently, a strong monopolar field. Conversely, a transverse field perpendicular to the blade will let

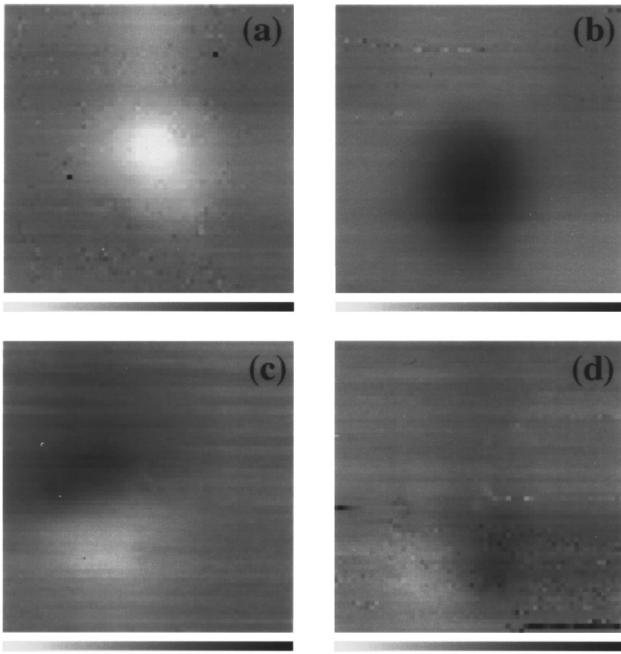


FIG. 3. Four different magnetizations of the same tip (170 nm coverage) give different Hall voltage maps (raw data, 6.4  $\mu\text{m}$  width, 64 points, the sensor is located roughly at the center of the images). The tip magnetization is (a) axial upwards, (b) axial downwards, (c) transverse, along the cantilever axis, and (d) transverse, perpendicular to the cantilever axis. The gray scale spans 460  $\mu\text{V}$  [(a), (b)] and 230  $\mu\text{V}$  [(c), (d)].

poles appear only on the back of the blade, and with opposite signs, giving rise to a weak dipolar tip field. In the pictures, especially those pertaining to an axial tip saturation, a non-uniform background may be seen, most probably an experimental artifact. One possible cause may, in view of the sensor sensitivity to light, be an incorrect centering of the laser beam (that reflects off the cantilever in order to monitor its deflection) on the cantilever. The two first pictures also clearly display an oval shape. This might be due to an asymmetric tip field profile, or to the fact that sensors are laid in close succession along one direction. But, it might also be an artifact, as the other images with a higher mesh size (0.21  $\mu\text{m}$ ) do not exhibit this phenomenon so clearly. The last two pictures have different extensions of the signal. The cause of that may be the nonsymmetrical shape of the pyramid, which was seen by scanning electron microscopy to be more extended parallel to the cantilever axis.

Before going into deeper details, two numerical estimates can be readily extracted out of the images. First, the axially saturated tip signals are of the same lateral size as the Hall cross. This means that the stray field extends over a region appreciably smaller than the sensor width. Second, the maximum signal for the axially saturated tip is about 0.2 mV, meaning that the sensor sees an average field equal to 30 Oe. If, for example, one assumes that this field is concentrated in a square of size 0.5  $\mu\text{m}$ , then the field is equal to 500 Oe. In the last reasoning, we have implicitly assumed that the Hall sensor, when subjected to an inhomogeneous field, responds as if submitted to a uniform field equal to the average of the inhomogeneous field over the central square.

The validity of this assumption is investigated in the following section.

### III. CALCULATION OF THE HALL VOLTAGE IN AN INHOMOGENEOUS FIELD

We consider only one cross having infinite arms of width  $a$  (Fig. 1). Let  $\sigma$  denote the layer conductivity,  $t$  its thickness, and  $n$  the carrier density (charge  $q$ ). In a first approximation, one may consider that the current density is everywhere parallel to the  $x$  axis, and uniform. It is, then, straightforward to show that the Hall voltage  $V_{\perp}$  induced by a uniform field  $B$ , and the potential difference  $V_{\parallel}$  along the  $I$  arm, for a length of  $Na$  (it contains  $N$  squares), are given by

$$V_{\perp} = (B/nqt)I, \quad V_{\parallel} = (N/\sigma t)I. \quad (1)$$

These expressions are independent of  $a$ , providing a strong argument in favor of the miniaturization of the Hall sensors. The Hall resistance  $R_H$ , defined as  $V_{\perp}/I$ , within this classical model, is perfectly linear in field. This current distribution causes the sensor to only respond to fields that exist in the central square, in a uniform way. Consequently, a global Hall voltage equal to that produced by a uniform field, given by the average value of the true field over the central square, is predicted.

It is, nonetheless, obvious that the current flow will sense the  $V$  arms extending on the sides, and enter them. We are, therefore, lead to admit that the field outside the central square will also contribute to the global Hall voltage. The current flow in the cross geometry admits an analytical solution in 2D (the limit when the layer thickness is much smaller than the cross width) within the framework of conformal mapping techniques.<sup>13</sup> Denoting by  $\mathbf{j}$  the (in-plane) current density vector,  $\mathbf{E}$  the (in-plane) electric field vector, and  $\mathbf{B}$  the (perpendicular) magnetic induction vector, the equations giving the stationary current flow are

$$\mathbf{j} = \sigma(\mathbf{E} + (1/nq)\mathbf{j} \times \mathbf{B}), \quad (2)$$

$$\text{div } \mathbf{j} = 0, \quad (3)$$

$$\text{rot } \mathbf{E} = \mathbf{0}. \quad (4)$$

Equation (2) represents the Ohm's law supplemented by the Lorentz force, Eq. (3) expresses the charge conservation, and Eq. (4) is the remaining Maxwell equation for the electric field. The other Maxwell equation for  $E$  is useless, for during the transient time where  $B$  is established, charge may build up at some places, creating a nonzero but unknown charge density.<sup>14</sup> In these equations,  $B$  denotes the external field, the field created by the current itself being neglected.<sup>15</sup> The solution of these equations, in the cross geometry, is exposed in the appendix. Figure 4 shows the field lines and the equipotential curves in the  $B=0$  case. The solution to first order in  $B$  ( $\sigma B/nq \ll 1$ ) is shown in Fig. 5. Plotted in gray levels or in height is the value of the elementary Hall voltage created by a Dirac  $\delta$  function for  $B$ , located at the point considered. Note that this solution is given in an analytical form, the preceding estimate<sup>16</sup> being only numerical. The analytical solution is in very close agreement with the earlier numerical calculation. In Fig. 5, one recognizes a nearly constant value in the central square. Its integral weight,

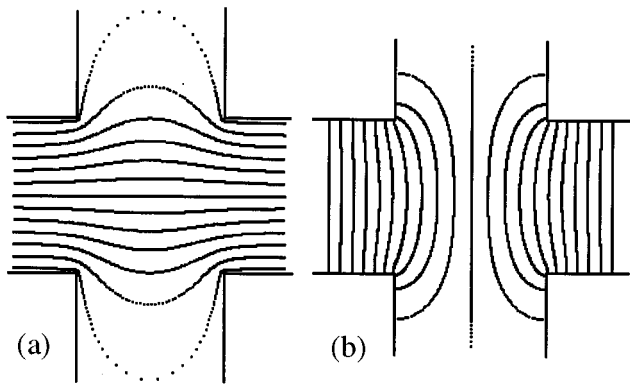


FIG. 4. 2D analytic calculation of the current distribution in the cross, in the absence of magnetic field. (a) current lines ( $U_0 = \text{constant}$ ) and (b) equipotential lines ( $V_0 = \text{constant}$ ). The constants are varying in increments of 0.5;  $U_0 = \pm \pi$  on the boundary.

however, is only equal to half of the total. The rest of the response comes from the four arms of the cross, where a near exponential decay of the response takes place, with a characteristic length roughly equal to one-third of the sensor width. Thus, only 1% of the global response comes from the central squares of the two neighboring sensors. The problem was not solved for a chain of sensors. An infinite chain would force the straight lines in between two successive sensors to be equipotentials. Figure 4(b) shows that this is nearly the case, so that only a small response function widening along the chain axis must take place. This disposes of one of the concerns about the origin of the oval shapes seen in Figs. 3(a) and 3(b).

The main assumption in the preceding calculation is that the sensor has such a sharp cross profile. Figure 2(a) shows a distinct rounding effect at the corners of the cross. Although we have not calculated it, we anticipate that this should remove the four tips of the response function at these points. Charge depletion at the conductor edges should, moreover, smear the results, so that the true response function should first be scaled down, and also transformed somehow from a ‘‘clergyman hat’’ to a standard ‘‘rounded top hat’’ form. A direct measurement of the response function would be helpful at this point. Punctual field sources are required to achieve that goal. MFM tips may be close to being punctual, but then, the whole problem would become circular since we precisely want to see how punctual they are. Therefore, in a first step, we shall use the calculated response map.

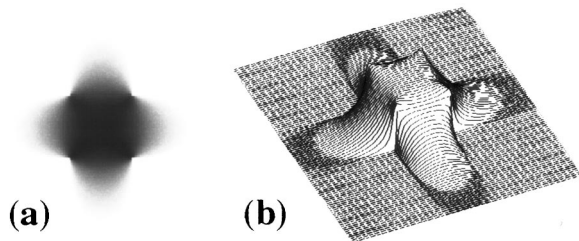


FIG. 5. 2D analytical calculation of the linear Hall effect in an inhomogeneous field (response function): (a) gray scale top view; and (b) bird's eye view. See the Appendix for the formulae.

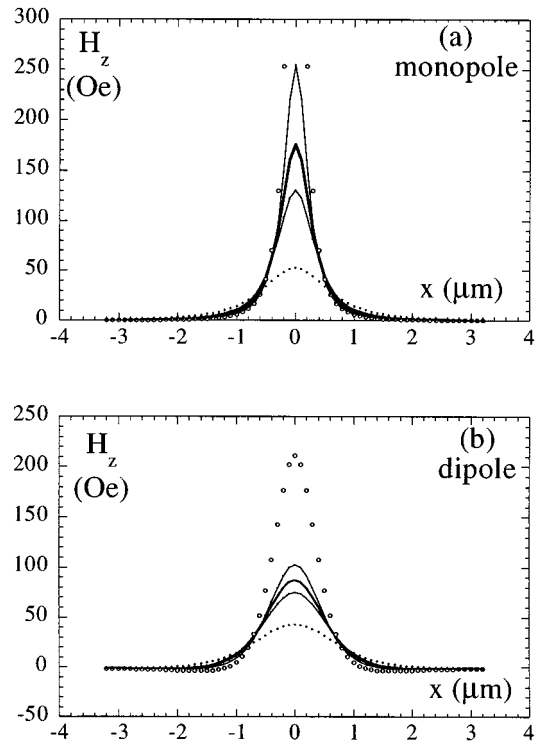


FIG. 6. (a) Least-squares fit of the Hall map of Fig. 3(a) with a tip modeled as a monopole with adjusted effective height above the sensor. Sensor size:  $2 \mu\text{m}$  (open symbols),  $1.5 \mu\text{m}$  (median curve), and  $1 \mu\text{m}$  (full symbols). A linear background is taken into account. The resulting effective heights ( $\mu\text{m}$ ) and residual errors ( $\mu\text{V}$ ) are, for decreasing sensor size, 0.22 and 17.5, 0.40 and 14.6, and 0.9 and 15.1. In the  $2 \mu\text{m}$  case, the fitted  $z$  field peaks at 622 Oe. The two other curves correspond to a sensor width of  $1.5 \mu\text{m}$ , with effective heights amounting to 0.32 and  $0.49 \mu\text{m}$ , which give rise to 14.7  $\mu\text{V}$  error values. (b) Least-squares fit of the Hall map of Fig. 3(a) with a tip modeled as a vertical dipole of adjusted effective height above the sensor. Sensor size:  $2 \mu\text{m}$  (open symbols),  $1.5 \mu\text{m}$  (median curve), and  $1 \mu\text{m}$  (full symbols). A linear background is taken into account. The resulting effective heights ( $\mu\text{m}$ ) and residual errors ( $\mu\text{V}$ ) are, for decreasing sensor size, 0.81 and 16.4, 1.11 and 14.1, and 1.6 and 14.3. The two other curves correspond to a sensor width of  $1.5 \mu\text{m}$ , with effective heights amounting to 1.00 and  $1.22 \mu\text{m}$ , which give rise to 14.2  $\mu\text{V}$  error values.

#### IV. DECONVOLUTION OF THE HALL VOLTAGE MAPS

A first processing of the Hall voltage map consists in assuming that the tip stray field has a given functional form, which depends on some parameters (a procedure similar to that of Ref. 9). These parameters are optimized by minimizing the norm of the difference between the measured and the calculated images. Reasonable functional forms are the field of a monopole, of a dipole, etc. Parameters are the strength of the multipole, its position above the surface, and the background level in the Hall voltage map. The optimization of the parameters entering the image difference in a nonlinear way has to be performed by iterations, but this calculation can still be fast. Figure 6 displays the results of a deconvolution of Fig. 3(a) taking the tip field to be that of a monopole [Fig. 6(a)], or a vertical dipole [Fig. 6(b)], with various assumed sensor sizes. The  $2 \mu\text{m}$  sensor width gives rise to nearly punctual deconvoluted field profiles, and therefore, to very high field values. But, assuming a  $1.5 \mu\text{m}$  sensor, the error greatly decreases and the field takes on a less punctual pro-

file. Trying a 1  $\mu\text{m}$  sensor increases the error anew, while appreciably widening the field profile and decreasing the field amplitude. The anomalous behavior of the deconvolution with 2  $\mu\text{m}$  width is to be ascribed to the fact that the response function is wider than the peak to deconvolve. We infer from this that the effective sensor size is closer to 1.5  $\mu\text{m}$  than to 2  $\mu\text{m}$ . For the 1.5  $\mu\text{m}$  sensor width, the two field profiles obtained under allowance of a 0.1  $\mu\text{V}$  error increase are also plotted. They give an idea of the “robustness” of the field profile.

The reasonable maximum field values are scattered around 100 Oe, depending on the assumed sensor size and tip model. To reduce this large scatter, one can relax the constraint imposed by the tip model. Far from the tip, the field distribution may fit well the assumed tip model. In close proximity of the tip, however, i.e. at a distance comparable to or smaller than the tip magnetic structure length scale, it is likely that many multipole terms become relevant. We, therefore, need a more general method.

In a second step, one looks for an unknown, *a priori* arbitrary, field map  $H(u,v)$  that would reproduce the image (Hall voltage map)  $I(x,y)$  according to the response function  $R$ . It has to satisfy

$$I(x,y) = \iint H(u,v)R(x+u-x_0,y+v-y_0)dudv. \quad (5)$$

Here,  $x_0$  and  $y_0$  denote the coordinates of the center of the Hall sensor, in the image frame. They can be estimated to be the center of the feature appearing in the image. Equation (5) is not a full equality, as noise is also present, so that the equality has to be solved in least squares. Our images are also discrete, consisting of  $NI \times NI$  ( $NI=64$ ) points with a spacing of 0.1  $\mu\text{m}$  (high resolution) or 0.2125  $\mu\text{m}$  (low resolution). A discrete  $H$  will, therefore, be sought, and one must take less points than in the image in order to get a reasonable solution. If the same mesh size is taken for  $H$  and for  $R$ , Eq. (5), in discrete form, reads

$$\text{for every } i,j \quad I(i,j) = \sum_k \sum_l H(k,l)R(i+k-i_0,j+l-j_0). \quad (6)$$

We take  $k$  and  $l$  running from  $-NC$  to  $NC$ , with  $NC=16$ , meaning that we have about four times more equations than unknowns. The rich literature on least-squares fitting<sup>17</sup> proposes many ways to solve Eq. (6). The most immediate one consists in minimizing the error norm  $E$  directly, by derivation with respect to every  $H(k,l)$ . The error is given by

$$E = \sum_{i,j} \left( I(i,j) - \sum_{k,l} H(k,l)R(i+k-i_0,j+l-j_0) \right)^2. \quad (7)$$

This results in a linear system, written in matrix form as ( $t$  denotes the transposed matrix)

$${}^tRRH = {}^tRI. \quad (8)$$

Unfortunately, the solution of Eq. (8) is almost completely noise, the small eigenvalues of  ${}^tRR$ , which is a positive definite matrix, being the cause of the problem. As a remedy,

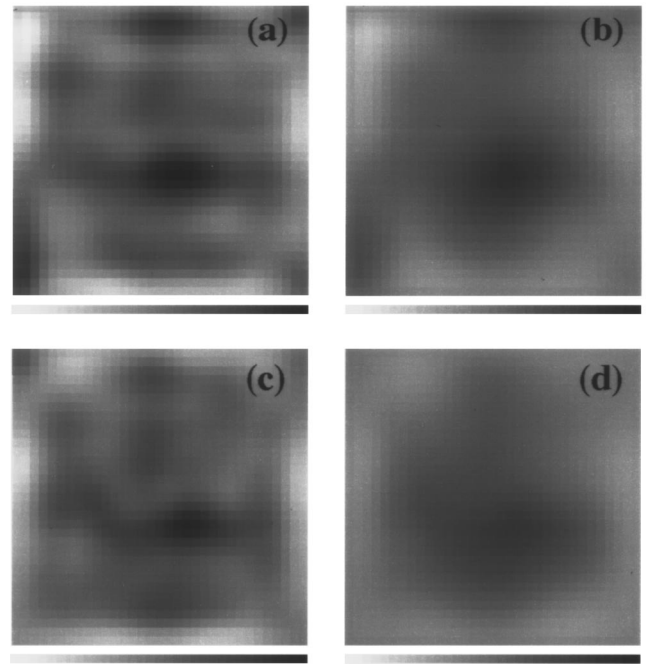


FIG. 7. Deconvolved  $z$  field maps corresponding to the Hall map of Fig. 3(a), using the Levenberg–Marquardt algorithm with field gradient penalization. Size  $33 \times 33$  points with a 0.1  $\mu\text{m}$  spacing, linear contrast from  $-200$  to  $+200$  Oe, the sensor being 2  $\mu\text{m}$  wide. The constant  $A$  characterizing the penalization is 100 [(a), (c)] or 1000 [(b), (d)]. For the second row, the lower left brighter part of the background of Fig. 3(a) was removed, and the image was radially averaged at distances larger than 2  $\mu\text{m}$  from the image center. A linear background is included. Residual errors are, in  $\mu\text{V}$ , (a): 11.5, (b): 12.1, (c): 9.5, and (d): 9.7.

one may add to the error defined by Eq. (7) a cost function for  $H$ , such as the sum of the squares of the elements of  $H$ , or the sum of the squares of the gradients of the field map, times some constant  $A$ . Such a procedure effectively suppresses the deconvolution noise, but also damps the signal, which becomes wider and weaker. That method is called the Levenberg–Marquardt algorithm.<sup>17</sup> Figure 7 shows the results of some deconvolutions of Fig. 3(a), with a cost function linked to the gradients of  $H$ . The gradient of the field was chosen because it allows us to enforce a zero field at the boundary of the field map, which is what we expect if the field is well localized and the map wide enough. The method is still fast, as it involves a positive definite matrix of moderate size, which is easily inverted. The error  $E$  has significantly decreased, and Fig. 7(a) contains much more details than the profiles of Fig. 6, obtained with the first deconvolution method. Choosing the  $A$  parameter *a priori* is a problem. A first guess is to take a compromise value, which suppresses most of the noise while still moderately damping the signal. Figure 7(b) shows the damping effect of a larger constant  $A=1000$ , compared to  $A=100$  [Fig. 7(a)]. The lower value is clearly more appropriate. One notices positive and negative peaks on the left part of the convoluted field map [Figs. 7(a) and 7(b)]. They are mainly due to background inhomogeneities. Indeed, if one averages radially the image above a certain distance from the peak center and deconvolves it, these spurious peaks are nearly removed [Figs. 7(c) and 7(d)]. A positive peak above the central one remains,

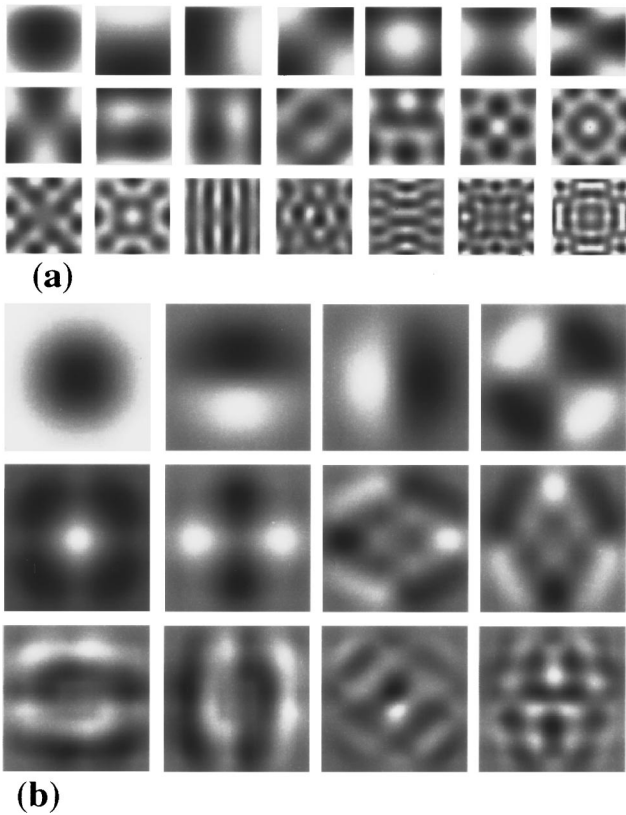


FIG. 8. Singular vectors corresponding to Fig. 3(b). (a)  $H$  space, the singular vectors are number 1–10, 15–40 (step 5), and 50–90 (step 10), the singular value falls from 425 to 4 between number 1 and 90 (the minimum singular value being 0.28 at number 1090); (b)  $I$  space, the singular vectors bear numbers 1–10, 15, and 20. A constant background is considered in this calculation.

nevertheless, present; it expresses the fact that the structure to deconvolve is extended vertically, as noted before. Thus, this method is rapid, but suffers from the number of its adjustable parameters (form and magnitude of the penalization). We, therefore, turn to the third, more rigorous, method.

Perhaps the finest method is that called singular value decomposition.<sup>17</sup> We come back to Eq. (6), i.e.,  $RH=I$  in matrix form, and find what are the equivalents of the eigenvalues of  $R$  (remember,  $R$  is not a square matrix). They are called singular values, and have associated to them singular vectors, both in  $I$  and  $H$  space. The singular values are all positive. Figure 8 shows some selected eigenvectors ( $I$  and  $H$  space) pertaining to Fig. 3(b), where the sensor was well centered. They satisfy the relation  $R\mathbf{h}_n = s_n \mathbf{i}_n$ , where  $s_n$  is the singular value of number  $n$ ,  $\mathbf{i}_n$  and  $\mathbf{h}_n$  the associated singular vectors in  $I$  and  $H$  space. The singular vectors show an increasing number of nodes for decreasing singular value. They look somehow like normal modes of a square drum.  $H$  is then reconstructed with a controlled noise amount by selecting only the vectors that have sufficiently high singular values. The cutoff is chosen by examination of the residual error, both of the norm of  $H$  and the norm of the  $I$  components (projections of  $I$  on the singular vectors in  $I$  space) compared to the noise level present in  $I$ . As before, selecting less singular values in the construction of the solution eliminates noise further, but also damps the signal more. This

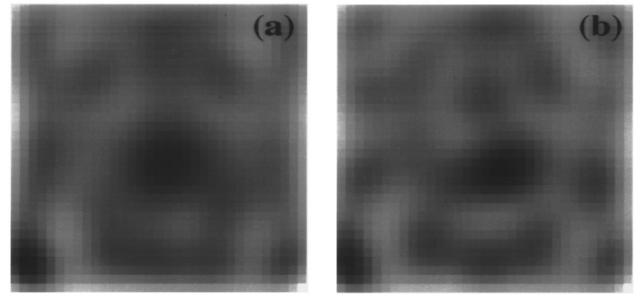


FIG. 9. Deconvolved  $z$  field maps corresponding to the Hall map of Fig. 3(a), using the singular value decomposition method. Size  $33 \times 33$  points with a  $0.1 \mu\text{m}$  spacing, linear contrast from  $-300$  to  $+200$  Oe, the sensor being  $2 \mu\text{m}$  wide. 40 singular values were retained for (a), and 60 for (b). A constant background is included. Residual errors are (a): 10.81 and (b): 10.76  $\mu\text{V}$ .

method is the most expensive in terms of computing power, as a large and nonsymmetric matrix has to be treated. Here, out of 1090 ( $33 \times 33 + 1$ , the background level), we retained about 40 singular modes, following the prescriptions described above. Figure 9 presents deconvolved images of Fig. 3(a), that have to be compared to Fig. 7. Some differences arise on the borders, because the field has been assumed in the calculation of the gradient penalization tube to be zero outside, thus, forcing the field to decrease at the borders. These images achieve lower errors compared to Fig. 7, but feature large negative and positive field peaks on the borders of the field map. Altogether, the finest method provides, by comparison, an independent way of choosing the constant  $A$  of the Levenberg–Marquardt method. It appears that the value  $A=100$ , which was determined above, provides field maps reasonably close to those of the third method. We shall use the second method in the following, owing to its rapidity (10 CPU min instead of 4 h).

## V. APPLICATION TO MFM THIN-FILM TIPS

### A. Variation of the magnetic film thickness

The Co–Cr layer thickness was decreased from 170 to 30 nm. The reduction of the associated stray field, in the axial saturation case, is directly evident on the maximum Hall signals (Table I). The signal width (full width at half-maximum) was nearly constant. The signal amplitude increases first linearly with the CoCr coating thickness, and then seems to saturate.

These results, in order to be interpreted, already require some ideas about the magnetization distribution in the tip. An important relation, in this respect, states that the integral over a planar surface of the perpendicular component of the field due to a monopole is equal to the solid angle under which the monopole sees that surface, times the monopole charge (Gauss theorem). Thus, the linear signal increase at small tip coverage, interpreted as due to the field of a monopole (a monopolar charge distribution well smaller than the sensor width) at a small distance from the sensor, means that this monopole strength increases linearly with tip coverage. This would imply that the magnetization lies in the plane of the various facets of the tip pyramid. The signal saturation

TABLE I. Effect of the tip coverage thickness on the Hall voltage signal.

CoCr coating thickness (nm)	Tip saturation direction	Average signal amplitude ( $\mu\text{V}$ )	Standard deviation ( $\mu\text{V}$ )	Number of images
170	axial	206	41	14
90	axial	160	0	1
50	axial	87	19	3
30	axial	55	15	2
170	transverse	105	14	6

at high coverage could come from a transition to a perpendicular magnetization in the facets, as is known to occur in Co–Cr recording media.<sup>18</sup> These guesses on the tip models are consistent with what emerges out of micromagnetic calculations.<sup>19</sup>

## B. Towards the field profiles of tips

As obvious from the previous paragraphs, the deconvolution process is extremely sensitive to background signals. The random noise is efficiently removed by the various algorithms, but not an uneven background or a distorted signal. It is, of course, possible to remove selectively some evident artifacts, but the risk of data distortion is rather high. One should, therefore, start from the cleanest Hall maps. In our case, these maps were obtained in the low resolution case (point spacing  $0.2125 \mu\text{m}$ ). Figure 2(b) is a typical and reproducible example of such maps; and we shall work below on a similar image with an inverse tip axial magnetization, for a better visualization of the field maps.

The practical problem we are faced with when deconvoluting is the choice of the effective sensor size. A close look at Fig. 2(b) reveals that the signal area is smaller than the nominal  $2 \mu\text{m}$  wide square. This results in a rather oscillating field profile [Fig. 10(a)], instead of the punctual profile found when constraining the field to be monopolar or dipolar. If the sensor size is reduced to  $1.5 \mu\text{m}$ , these oscillations are reduced, the error  $E$  falls, and the maximum field rises a little [Fig. 10(b)]. Further reduction of the sensor size to  $1 \mu\text{m}$  wipes out all oscillations, but reduces the maximum field and starts increasing the error [Fig. 10(c)], although that error increase was not systematic. The tendency of the field to decrease when the sensor size is reduced down to zero is easy to understand. At zero sensor size, the deconvolved field is simply the Hall voltage profile divided by the sensitivity [Fig. 10(d)], and if the sensor size increases from zero, the field profile becomes sharper and higher (up to the point where the sensor size becomes larger than that of the signal). Thus, it is hard to infer from the images what the effective sensor size is; only an upper bound can be estimated from the size of the signal seen, provided that the field profile is simple (bell shaped). Here, under the hypothesis that the response function is such as calculated, we find that the effective sensor size is smaller than the expected  $2 \mu\text{m}$  value, and probably around  $1.5 \mu\text{m}$ .

The deduced peak field values, at a distance close to 100 nm from the tips contact surface, are about 100 Oe for the tip with the thickest coverage (170 nm), falling to about 30 Oe at the thinnest coverage (30 nm). As the preceding consider-

ations have shown that, from the images obtained with our present sensors, the fine details of the field profile are not established firmly enough, we do not attempt to interpret them in terms of tip models. This is clearly the next step to be taken. For that, images devoid of any artifacts are crucial.

## VI. CONCLUSION

We have experimentally and theoretically investigated the reconstruction of an inhomogeneous field profile from a set of measurements by a Hall sensor of finite size. The primary application was the study of the field emitted by magnetic force microscope tips, but the method is quite general. For any deconvolution, the response function of the instrument is required. We have calculated that of an idealized sensor (two-dimensional, perfect shape, no edge depletion), and used that result for the deconvolution. Experimental results suggest that a significant edge depletion occurs, reducing the sensor width from 2.2 to about  $1.5 \mu\text{m}$ . As there is no direct measurement of the response function, some uncertainty affects the deconvoluted field profiles. Despite this

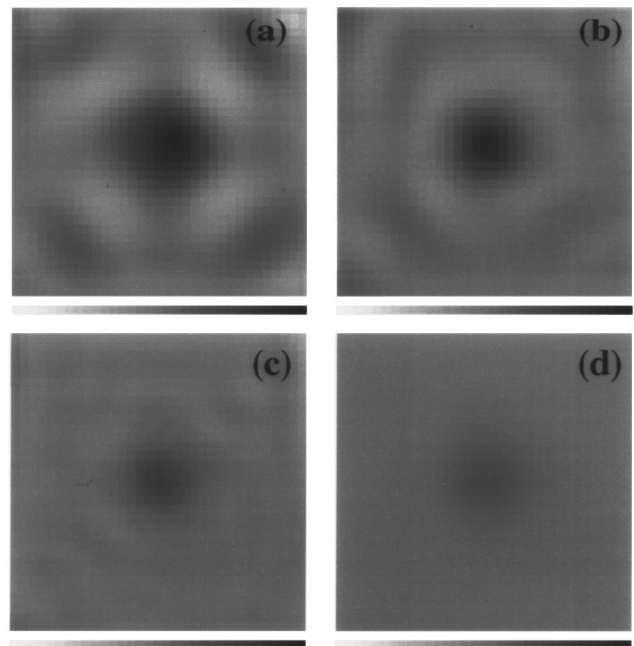


FIG. 10. Deconvolved  $z$  field maps by the Levenberg–Marquardt algorithm, corresponding to a Hall map similar to Fig. 2(b), the tip having been magnetized in the opposite direction. The constant  $A$  is equal to 100, the linear contrast scale is  $-100$  to  $100$  Oe,  $33 \times 33$  points with a  $0.2125 \mu\text{m}$  step. A linear background is included. Sensor sizes are (a)  $2.0$ , (b)  $1.5$ , (c)  $1.0 \mu\text{m}$ , and (d) punctual. The respective errors are 7.3, 6.3, 6.5, and  $7.0 \mu\text{V}$ .

limitation, a number of features of the field emitted by the measured magnetic force microscope tips have been obtained. The use of smaller Hall sensors, i.e., with an effective width equal to the resolution desired, would remove the need for a deconvolution and produce directly a lightly smoothed field profile. How feasible this is, and down to which size, remains to be investigated.

## ACKNOWLEDGMENTS

The authors thank H. Shtrikman (Weizmann Institute) for the preparation of the GaAs/AlGaAs heterostructures. One of the authors (A.T.) acknowledges stimulating discussions with P. Bruno, J. Caulet, and C. Chappert (IEF, Orsay) concerning the analytic calculation of the response function.

## APPENDIX: ANALYTIC CALCULATION OF THE RESPONSE FUNCTION

The starting equations are Eqs. (2)–(4), supplemented by the boundary condition  $\mathbf{j} \cdot \mathbf{n} = 0$  ( $\mathbf{t}$  denotes the local tangent to the boundary, oriented in the direct sense, and  $\mathbf{n}$  is the outwards normal). Equation (4) is solved by introducing the electrostatic potential  $V: \mathbf{E} = -\mathbf{grad} V$ . Let us also denote by  $\beta$  the scalar function  $\sigma B/nq$ . The system transforms to

$$(1 + \beta^2)\Delta V + (1 - \beta^2)\left(\frac{\partial\beta}{\partial x}\frac{\partial V}{\partial y} - \frac{\partial\beta}{\partial y}\frac{\partial V}{\partial x}\right) - 2\beta\left(\frac{\partial\beta}{\partial x}\frac{\partial V}{\partial x} + \frac{\partial\beta}{\partial y}\frac{\partial V}{\partial y}\right) = 0 \quad \text{inside}, \quad (\text{A1})$$

$$\frac{\partial V}{\partial n} = -\beta \frac{\partial V}{\partial t} \quad \text{on the boundary}. \quad (\text{A2})$$

In the limit  $\beta \ll 1$  ( $B \ll 3000$  Oe, here), it is natural to expand  $V$  in powers of  $\beta$ ;  $V = V_0 + V_1 + \dots$ , where  $V_0$  is the solution of the zero-field problem given by

$$\Delta V_0 = 0 \quad \text{inside}, \quad (\text{A3})$$

$$\frac{\partial V_0}{\partial n} = 0 \quad \text{on the boundary}, \quad (\text{A4})$$

and  $V_1$  satisfies

$$\Delta V_1 = \frac{\partial\beta}{\partial y}\frac{\partial V_0}{\partial x} - \frac{\partial\beta}{\partial x}\frac{\partial V_0}{\partial y} \quad \text{inside}, \quad (\text{A5})$$

$$\frac{\partial V_1}{\partial n} = -\beta \frac{\partial V_0}{\partial t} \quad \text{on the boundary}. \quad (\text{A6})$$

### A. Solution of the $V_0$ problem

Equations (A3) and (A4) are the standard Poisson equations. As we did not find the solution of the infinite arms cross in the literature, and because this solution is needed for the  $V_1$  problem, we now sketch the derivation of  $V_0$ . We define the complex variables<sup>13</sup>  $z = x + iy$ ,  $W_0 = V_0 + iU_0$ , where  $U_0$  is the conjugate function of  $V_0$  (the current function). Any analytic function  $W_0(z)$  provides a solution of Eq. (A3). To fulfill Eq. (A4), we look for an analytic transformation  $z \rightarrow \zeta$  that transforms the boundary into the real axis of the complex plane. To simplify, we use the symmetry and

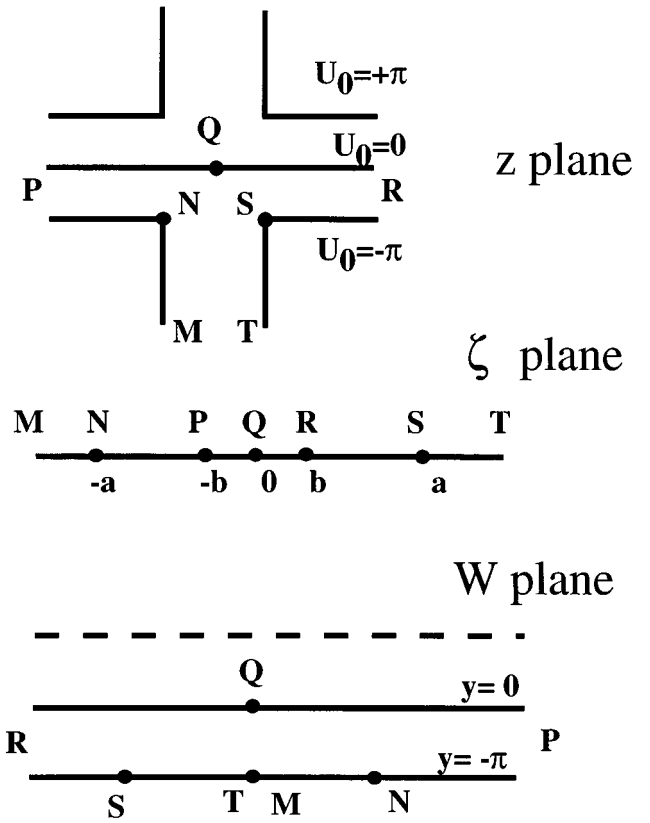


FIG. 11. Schematic of the successive transformations in the complex plane for the solution of the potential problem.

consider only the lower half of the cross (Fig. 11). The potential is scaled by a constant such that  $U_0$  is equal to  $\pm\pi$  on the boundary.

The general transformation applying to this boundary shape is given by<sup>13</sup>

$$\frac{dz}{d\zeta} = C^{\text{st}i} \frac{\sqrt{\zeta^2 - a^2}}{\zeta^2 - b^2}, \quad (\text{A7})$$

where  $a$ ,  $b$ , and the constant are to be found so that the points  $M$  to  $T$  fall at the desired places. Equation (A7) integrates into

$$z = D + iC \left\{ 2b \log(\zeta + \sqrt{\zeta^2 - a^2}) + \sqrt{a^2 - b^2} \left[ \arctan\left(\frac{\sqrt{a^2 - b^2}\sqrt{\zeta^2 - a^2}}{b\zeta - a^2}\right) + \arctan\left(\frac{\sqrt{a^2 - b^2}\sqrt{\zeta^2 - a^2}}{b\zeta + a^2}\right) \right] \right\}. \quad (\text{A8})$$

The cross described by Eq. (A8) is rectangular, with sizes  $2\pi Cb$  in  $x$  and  $2\pi C(a^2 - b^2)^{1/2}$  in  $y$ . For the square cross  $C = -1/\pi$ ,  $b = 1$ ,  $a = \sqrt{2}$ , and  $D = -1$ . The second transformation

$$W = \log\left(\frac{\zeta - 1}{\zeta + 1}\right) - i\pi, \quad (\text{A9})$$

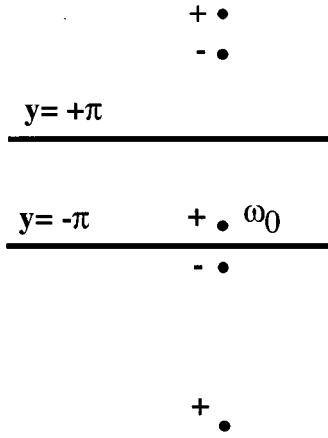


FIG. 12. The images of point  $\omega_0 = W(z_0)$  in the  $W$  plane that allow the fulfillment of the boundary condition (A6) for the  $V_1$  problem in the cross geometry pertaining to a field distribution given by a Dirac delta function located at  $z_0$ .

maps the real axis in the  $\zeta$  plane into two horizontal lines at  $U = -\pi$  and  $U = 0$  in the  $W$  plane. In that  $W$  plane, the solution of Eq. (A4) with the given  $U_0$  values is, evidently,  $W_0 = W$ . This completes the solution of the potential to the zeroth order. The calculated equipotential lines ( $V_0 = \text{constant}$ ) and current lines ( $U_0 = \text{constant}$ ) are drawn in Fig. 4; they look as expected, 20% of the current goes through the  $V$  arms, avoiding the central square.

## B. Solution of the $V_1$ problem

From Eqs. (A5) and (A6), one sees that the superposition principle holds, due to the first-order approximation. Let us, therefore, consider that  $B$  is a Dirac delta function  $\beta = \delta(x - x_0)\delta(y - y_0)$ . The solution of Eq. (A5) in infinite space is readily found to be

$$W_1 = \frac{1}{2\pi} \frac{i}{\bar{z} - \bar{z}_0} \frac{dW_0}{dz} \Big|_{z=z_0}. \quad (\text{A10})$$

One has, moreover, to fulfill the boundary condition (A6), namely  $\partial V_1 / \partial n = 0$  ( $z_0$  is inside the cross). It is more convenient to solve this problem in the  $W$  space, where the boundary of the whole cross is given by the two lines  $U = \pm\pi$ . In this change of variables, the Dirac delta function will be multiplied by the Jacobian  $|dW/dz|^2$ . To satisfy Eq. (A6), images have to be introduced as drawn in Fig. 12. Using the complex summation formula

$$\sum_{n=-\infty}^{+\infty} \frac{1}{z - 2ni\pi} = \frac{1}{e^z - 1},$$

one finds, after some rearrangement ( $\omega_0$  is the point corresponding to  $z_0$  in the  $W$  plane),

$$W_1 = \frac{i}{4\pi} \left| \frac{dW}{dz} \right|_{z_0}^2 \frac{ch(\bar{\omega}_0/2)}{sh(\bar{W}(z)/2) - sh(\bar{\omega}_0/2)}. \quad (\text{A11})$$

The derivative of  $W$  is, from Eqs. (A7) and (A9), given by  $dW/dz = i\pi/(\zeta^2 - 2)^{1/2}$ , and thus,

$$V_1(z) = \frac{\pi}{2|\zeta_0^2 - 2|} \text{Im} \left[ \frac{ch(\omega_0/2)}{sh(W(z)/2) - sh(\omega_0/2)} \right].$$

The Hall voltage is measured between the two  $V$  arms, at infinity where  $W = \pm i\pi$ , so that

$$V_{\text{Hall}} = \frac{\pi}{2|\zeta_0^2 - 2|} \text{Re} \left[ \frac{1}{ch(\omega_0/2)} \right] = \frac{\pi}{2} \frac{\text{Im} \sqrt{\zeta_0^2 - 1}}{|\zeta_0^2 - 2|}. \quad (\text{A12})$$

Thus, we have obtained an analytic formula for the response function, in parametric form through  $\zeta$ .

The result of a numerical evaluation of Eqs. (A8) and (A12) is plotted in Fig. 5. One can check numerically from Fig. 5, and analytically from Eqs. (A8) and (A12), that the integral of the response function over the whole cross is equal to  $2\pi$ . This result is evident, as the solution of Eqs. (A5) and (A6) in a uniform unit field ( $\beta = 1$ ) is  $V_1 = U_0$ . The numerical solution displays a symmetry between the  $I$  and  $V$  branches, i.e., it is not possible from the response function to know which branch carried the current. This symmetry is expected from very general reciprocity arguments.<sup>20</sup> In the calculation, that symmetry was broken during the transformation of  $z$  into  $\zeta$ . But if Eq. (A8) is rewritten by expressing the arctan function in terms of the complex logarithm, the transformation of  $\zeta$  into  $\zeta/(\zeta^2 - 1)^{1/2}$  appears to change  $z$  into  $iz$ , and leaves the Hall voltage invariant. The solution is, thus, truly symmetric.

Compared to the analytic solution<sup>14</sup> for the ‘‘Hall generator’’ (i.e., only a square), we see that the infinities of the response function at the corners have disappeared, the corner value being, namely,  $\pi/4$  in the infinite square cross case.

Finally, it is immediate to extend Eq. (A12) to the rectangular cross case. When the rectangle aspect ratio  $R$  departs from unity, a dip appears in the center, the weights of the central rectangle and thin branch decrease, while that of the thick branch increases. The corner value is now  $\pi/(4R)$ , whereas the center value is  $\pi/(2(R^2 + 1)^{1/2})$ . The important property of the square, namely, the near constancy of the response function in the central square is, therefore, lost in the rectangle case. This fact might affect the interpretation of measurements performed on rectangles.

<sup>1</sup>For a review, see P. Grütter, H. J. Mamin, and D. Rugar, in *Scanning Tunneling Microscopy II*, edited by R. Wiesendanger and H. J. Güntherodt (Springer, Berlin, 1992), pp. 151–207.

<sup>2</sup>W. Rave, R. Schäfer, and A. Hubert, *J. Magn. Magn. Mater.* **65**, 7 (1987).

<sup>3</sup>C. D. Wright and E. W. Hill, *Appl. Phys. Lett.* **67**, 433 (1995).

<sup>4</sup>W. Rave, L. Belliard, M. Labrune, A. Thiaville, and J. Miltat, *IEEE Trans. Magn.* **30**, 4473 (1994).

<sup>5</sup>S. Müller-Pfeiffer, M. Schneider, and W. Zinn, *Phys. Rev. B* **49**, 15 745 (1994); S. L. Tomlinson and E. W. Hill, *J. Magn. Magn. Mater.* **161**, 385 (1996).

<sup>6</sup>D. Rugar, H. J. Mamin, P. Guethner, S. E. Lambert, J. E. Stern, I. McFadyen, and T. Yogi, *J. Appl. Phys.* **68**, 1169 (1990).

<sup>7</sup>P. Grütter, D. Rugar, H. J. Mamin, C. Castillo, C.-J. Lin, I. R. McFadyen, and R. M. Valletta, *J. Appl. Phys.* **69**, 5883 (1991).

<sup>8</sup>G. Matteucci, M. Muccini, and U. Hartmann, *Phys. Rev. B* **50**, 6823 (1994).

<sup>9</sup>D. G. Streblichenko, M. R. Scheinfein, M. Mankos, and K. Babcock, *IEEE Trans. Magn.* **32**, 4124 (1996).

<sup>10</sup>K. Sueoka, F. Sai, K. Parker, and T. Arnoldussen, *J. Vac. Sci. Technol. B* **12**, 1618 (1994).

<sup>11</sup>A. M. Chang, H. D. Hallen, L. Harriott, H. F. Hess, H. L. Kao, J. Kwo, R.

- E. Miller, R. Wolfe, J. van der Ziel, and T. Y. Chang, *Appl. Phys. Lett.* **61**, 1974 (1992).
- <sup>12</sup>A. Oral, S. J. Bending, and M. Henini, *Appl. Phys. Lett.* **69**, 1324 (1996).
- <sup>13</sup>For a general presentation of the conformal mapping technique, see J. Jeans, *The Mathematical Theory of Electricity and Magnetism* (Cambridge University Press, Cambridge, 1951).
- <sup>14</sup>I. Hlasnik and J. Kokavec, *Solid-State Electron.* **9**, 585 (1966).
- <sup>15</sup>A current of intensity  $I$  flowing along a strip of width  $a$  and thickness  $t$  creates inside the strip a maximum induction  $B = \mu_0 I / (2\pi a) \ln(2ae/t)$ .
- With the present values  $a = 2 \mu\text{m}$ ,  $t = 400 \text{ \AA}$ , and  $I = 0.1 \text{ mA}$ , the maximum induction amounts to 0.5 G.
- <sup>16</sup>B. C. Webb and S. Schultz, *IEEE Trans. Magn.* **24**, 3006 (1988).
- <sup>17</sup>C. L. Lawson and R. J. Hanson, *Solving Least Squares Problems* (Prentice-Hall, Englewood Cliffs, NJ, 1974).
- <sup>18</sup>T. M. Coughlin, J. H. Judy, and E. R. Wuori, *IEEE Trans. Magn.* **17**, 3169 (1981).
- <sup>19</sup>S. L. Tomlinson and E. W. Hill, *J. Magn. Magn. Mater.* **161**, 385 (1996).
- <sup>20</sup>I. J. van der Pauw, *Philips Res. Rep.* **13**, 1 (1958).